Non-Cartesian sampled centric scan SPRITE imaging with magnetic field gradient and $B_0(t)$ field measurements for MRI in the vicinity of metal structures

Hui Han [a], Derrick Green [a,b], Matthew Ouellette [a], Rodney MacGregor [a], Bruce J. Balcom [a,*]

[a] MRI Centre, Department of Physics, University of New Brunswick, Fredericton, New Brunswick, Canada E3B 5A3
[b] Green Imaging Technologies, 2024 Lincoln Road, Fredericton, NB, Canada E3B 8M7

ARTICLE INFO

ABSTRACT

This paper proposes the possibility of spatially resolved MRI measurements undertaken inside metallic cells. MRI has been rarely usable inside conducting vessels due to the eddy currents in the walls caused by switching magnetic field gradients, which render most advanced MRI pulse sequences impossible. We propose magnetic field gradient waveform monitoring (MFGM) for MRI of samples inside metallic cells. In this work the MFGM method was extended to measure the B_0 field temporal evolution associated with gradient waveforms. MFGM was used to observe and correct eddy current effects associated with a metallic cell. High quality centric scan SPRITE images result from such corrections.

MRI of samples held under pressure, most notably rock core samples, traditionally employs cells that are non-magnetic and fabricated from polymeric materials. The natural material for high-pressure MRI is however non-ferromagnetic metal given their high tensile strengths and high thermal conductivity. MRI measurement of macroscopic samples at high pressure would be generally possible if metallic pressure vessels could be employed. This study will form the basis of new MRI compatible metallic pressure vessels, which will permit MRI of macroscopic systems at high pressure.

© 2010 Elsevier Inc. All rights reserved.

1. Introduction

This paper proposes the possibility of spatially resolved MRI measurements undertaken inside large scale metallic cells. MRI has been rarely usable inside conducting vessels due to the eddy currents in the walls caused by switching magnetic field gradients, which render most advanced MRI pulse sequences impossible. We propose magnetic field gradient waveform monitoring (MFGM) for MRI of samples inside metallic cells. In this work the MFGM method was extended to measure the B_0 field temporal evolution associated with gradient waveforms. MFGM was used to observe and correct eddy current effects associated with a metallic cell. High quality centric scan SPRITE images result from such corrections. This study will form the basis of new MRI compatible metallic pressure vessels, which will permit MRI of macroscopic systems at high pressure.

Since proposed in the early 1950s [1], high pressure NMR spectroscopy has been applied to a wide spectrum of problems in chemistry [2,3], bioscience [4], and material science [5]. However high-pressure MRI has been rare due to a low signal-to-noise ratio which results from a low filling factor and the restricted volume of commonly employed high-pressure cells [2–4]. MRI experiments

[5–8] using traditional high-pressure cells [2,3], are hindered by this problem, and inefficient temperature control [2,3,9].

Conventional high-pressure measurements in most scientific fields rely on metal vessels given the superior tensile strengths of metals. MRI measurement of macroscopic samples at high pressure would be generally possible if metallic pressure vessels could be employed. The high thermal conductivity of metals also makes them a natural choice for MRI compatible cells.

The critical problem with MRI compatible metallic cells is large scale, gradient induced eddy currents in metal, which will alter the desired magnetic field gradient waveform across the sample. As a consequence most MRI measurements will be rendered impossible or very difficult, especially advanced MRI pulse sequences which rely on large amplitude and fast slew-rate gradients.

Compared to clinical MRI, order of magnitude higher gradient strengths (up to 1000 mT/m) and up to two orders of magnitude greater net temporal gradient areas (up to several thousands ms mT/m), are often employed for non-medical MRI applications [10,11]. In material science MRI, gradient waveforms may range in duration from hundreds of milliseconds to several seconds. While a number of gradient/eddy current characterization methods exist in the literature [12–15], most are restricted to clinical use and are not suitable for this study due to the signal loss caused by large gradient dephasing and T_2^* decay [16].

These requirements can be well met by our recently proposed magnetic field gradient waveform monitor (MFGM) method [16]. The MFGM method uses a small RF probe (<1 cm with RF shielding) to temporally and/or spatially map the gradient behavior inside a limited sample space. The continuous RF pulsing of MFGM allows infinitely long duration waveforms to be measured with no limitation on sample T_2^* decay. MFGM avoids gradient dephasing by decomposing the large gradient area of a gradient waveform into small separate gradient areas with a short phase encoding time t_p. Large net gradient area and high gradient strengths can therefore be readily measured.

In this work the MFGM method was extended to measure the B_0 field temporal evolution associated with gradient waveforms. Improved MFGM was used to observe and correct the eddy current effects with a mock metallic cell. Quantitative centric scan SPRITE imaging including 1D DHK SPRITE [17] and 2D Spiral SPRITE [18,19], was successfully achieved with appropriate eddy current corrections. Linear eddy currents [25] are accounted for in the image reconstruction with monitored gradient waveforms. Linear eddy currents generate an additional linear magnetic field gradient that is superimposed upon the original magnetic field gradient produced by the gradient coil [25]. The B_0 field temporal evolution due to B_0 eddy currents was fixed in k-space, using a point-by-point phase correction algorithm.

1D quantitative imaging of fluid density is highly desirable in a wide variety of porous media measurements [20]. As a robust quantitative imaging technique, DHK SPRITE has been applied in the study of problems in food science [21], chemistry [22], and material science [23]. Centric scan SPRITE is recognized as the most efficient quantitative MR imaging technique in material science [18,19]. Compared with single point imaging (SPI) [24], the SPRITE sequence employs ramped gradient waveforms that permit image acquisition at a greater speed and minimizes gradient vibration due to impulsive Lorentz forces. Centric scan SPRITE is the most commonly implemented version of the SPRITE experiment.

As shown in this paper gradient waveforms are corrupted in the presence of large metallic structures but high quality images still result with gradient waveform measurement and k-space gridding.

2. Theory

2.1. Gradient waveforms and $B_0(t)$ field measurements

The pure phase encode magnetic field gradient monitor (MFGM) [16] employs a small RF probe to temporally map gradient waveforms for MR/MRI applications. One MFGM RF probe is displaced from the gradient isocenter inside the sample space to map linear gradient eddy currents and $B_0(t)$ eddy currents.

For the MFGM RF probehead displaced to spatial location r_n, the FID single point phase at a specific time t during a gradient waveform is

$$\varphi_n(t) = \varphi_{0,n} + \gamma \Delta B_0(t) t_p + \gamma t_p \mathbf{G}(t) r_n + \mathbf{O}(r_n^2), \tag{1}$$

where t_p is the phase encoding time (10–100 μs) between each RF excitation and subsequent FID single point detection [16]. $\varphi_{0,n}$ describes a constant phase offset. $\Delta B_0(t)$ is the spatially-constant field evolution. $\mathbf{G}(t) = [G_x(t), G_y(t), G_z(t)]$ represents the spatially-linear field, i.e., the gradient waveforms along three axes. $\mathbf{O}(r_n^2)$ is the spatially-nonlinear higher-order field terms.

Static magnetic field spatial variation, i.e., $\Delta B(r)$, resulting usually from main field inhomogeneity, chemical shift, and susceptibility differences, leads to a constant phase offset $\varphi_{0,n}$. $\varphi_{0,n}$ is obtained from baseline RF measurements prior to gradient waveform measurement. An extra scan is not required for baseline phase measurement [16].

The dynamic field may be decomposed by Taylor series expansion [25] into the spatially-constant term (zero-order, i.e., $\Delta B_0(t)$), the linear field (first-order, i.e., gradient $\mathbf{G}(t)$), and higher-order non-linear field terms in Eq. (1). Since the dynamic field components usually result from relatively distant sources outside the sample, e.g., the cryostat, gradient coils, and surrounding conductive structures, their fields vary smoothly across the sample space and can be well defined by relatively few spatial terms [15,26].

Most eddy current related image-quality problems can be traced to the zero-order and the first-order field terms in Eq. (1) [25]. For a 2D imaging application (assuming an x, y image), three spatial locations ($n = 3$) of an RF probehead are required to record $\Delta B_0(t)$, $G_x(t)$, and $G_y(t)$, which will account for magnetic field imperfections such as B_0 eddy currents, linear eddy currents, and gradient timing delays.

In order to extract, for example, $\Delta B_0(t)$, $G_x(t)$, and $G_y(t)$ information from Eq. (1) with $n = 3$, pre-calibration scans prior to the waveform mapping pulse sequence are required to determine the ratios between the spatial locations (r_n) of the RF probehead, i.e.,

$$\begin{aligned} \varepsilon_{x,ij} &= x_i/x_j & i &= 1, 2, 3 \\ \varepsilon_{y,ij} &= y_i/y_j & j &= 1, 2, 3 \end{aligned} \tag{2}$$

The calibration measurement is similar to the waveform mapping measurement [16] except for application of a constant gradient. After a long delay for eddy current decay and gradient stabilization, the phase acquired in Eq. (1) is determined by:

$$\phi_n(t) = \gamma t_p G_x \cdot x_n \tag{3}$$

where $\phi_n(t)$ is the FID single point phase $\varphi_n(t)$ offset by the baseline phase [16]. Therefore x_i/x_j equals ϕ_i/ϕ_j with the uncertainties in both t_p and G_x cancelled out.

Pre-calibration scans permit one to measure spatial ratios $\varepsilon_{x,ij}$ and $\varepsilon_{y,ij}$ very accurately. Unlike conventional gradient measurement methods [12–15], MFGM does not require accurate probe mounting and accurate measurement of locations (r_n). The ratios x_i/x_j and y_i/y_j can be measured with a higher accuracy than r_i because the uncertainties in other factors (e.g., the gradient strength) are cancelled out in the calculation. This avoids the phase errors that result from inaccuracy in calibrating probe spatial locations.

$\Delta B_0(t)$, $G_x(t)$, and $G_y(t)$ at any time point in the gradient waveform can be extracted by combining Eqs. (1) and (2). Assume that $\phi_n(t)$ is the FID single point phase, with the baseline phase subtracted [16], for the MFGM measurement at spatial location r_n, i.e., $\phi_n(t) = (\phi_n(t) - \phi_{0,n})$. Neglecting high-order field terms $\mathbf{O}(r_n^2)$ and substituting Eq. (2) into Eq. (1) provide for $n = 3$,

$$\phi_1(t) = \gamma \Delta B_0(t) t_p + \gamma t_p G_x(t) x_1 + \gamma t_p G_y(t) y_1 \tag{4}$$

$$\phi_2(t) = \gamma \Delta B_0(t) t_p + \gamma t_p G_x(t) x_1 \varepsilon_{x21} + \gamma t_p G_y(t) y_1 \varepsilon_{y21} \tag{5}$$

$$\phi_3(t) = \gamma \Delta B_0(t) t_p + \gamma t_p G_x(t) x_1 \varepsilon_{x31} + \gamma t_p G_y(t) y_1 \varepsilon_{y31} \tag{6}$$

Subtracting appropriate linear combinations of Eqs. (4)–(6) yields $\Delta B_{0(t)}$,

$$\Delta B_0(t) = \frac{(\varepsilon_{x21}\phi_1(t) - \phi_2(t))(\varepsilon_{x31} - \varepsilon_{y31}) - (\varepsilon_{x31}\phi_1(t) - \phi_3(t))(\varepsilon_{x21} - \varepsilon_{y21})}{\gamma t_p \left[(\varepsilon_{x21} - 1)(\varepsilon_{x31} - \varepsilon_{y31}) - (\varepsilon_{x31} - 1)(\varepsilon_{x21} - \varepsilon_{y21})\right]} \tag{7}$$

Similar manipulations of Eqs. (4)–(6) yield Eqs. (8) and (9), the expressions for magnetic field gradient x and y,

$$G_x(t) = \frac{(1 - \varepsilon_{y31})(\phi_1(t) - \phi_2(t)) - (1 - \varepsilon_{y21})(\phi_1(t) - \phi_3(t))}{\gamma t_p x_1 \left[(1 - \varepsilon_{x21})(1 - \varepsilon_{y21}) - (1 - \varepsilon_{x31})(1 - \varepsilon_{y31})\right]} \tag{8}$$

$$G_y(t) = \frac{(1 - \varepsilon_{x31})(\phi_1(t) - \phi_2(t)) - (1 - \varepsilon_{x21})(\phi_1(t) - \phi_3(t))}{\gamma t_p y_1 \left[(1 - \varepsilon_{x31})(1 - \varepsilon_{y21}) - (1 - \varepsilon_{x21})(1 - \varepsilon_{y31})\right]} \tag{9}$$
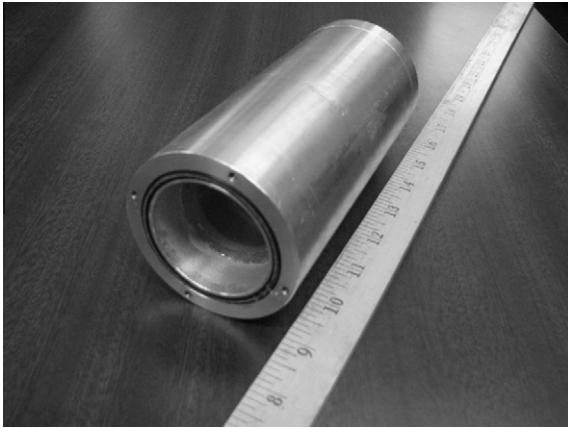
Fig. 1. A mock pressure vessel was fabricated using aluminum to verify the idea of MR imaging within metal cells. Imaging was undertaken with an RF coil which was within the aluminum cell.

Fig. 2. Measured rectangular gradient pulse and the concomitant B_0 eddy currents inside the aluminum cell (Fig. 1) using the magnetic field gradient waveform monitor (MFGM) method. Input rectangular gradient pulse shape (– – –), measured gradient shape (—), and measured $B_0(t)$ field (• • •). The gradient rise time from 10% to 90% was as long as 10 ms due to the high electrical conductivity and thickness of the cell walls. Note in the inset figure the positive lobe of the induced B_0 eddy currents is lower than the negative lobe due to an eddy current cancellation effect.

In Eqs. (8) and (9), the sample location x_1, y_1 need not be known exactly because one plots the gradient waveform by scaling the measured phases to the phase of a known time-invariant gradient [16].

2.2. Non-Cartesian sampled centric scan SPRITE

Centric scan SPRITE [8,17–19,21–23] is a robust quantitative imaging methodology ideally suited for studying short lifetime species (e.g., fluids in porous media). For simplicity in image reconstruction, all SPRITE techniques sample k-space on Cartesian grids by applying specifically designed gradient waveforms in a stepwise manner. In the presence of severe eddy currents (e.g., due to metal-
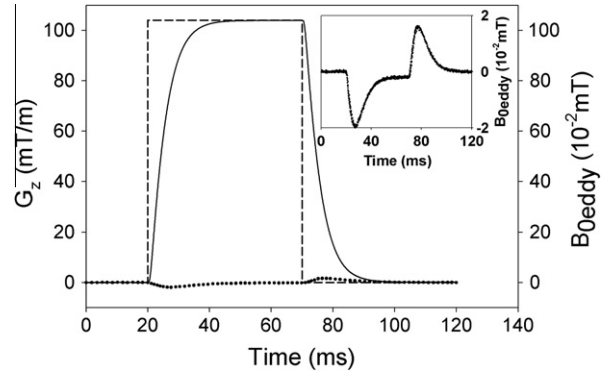
lic vessels) SPRITE k-space samples may deviate from the Cartesian grid due to gradient waveform distortions. Centric scan 1D DHK SPRITE and 2D Spiral SPRITE are the most widely used SPRITE measurements for 1D and 2D acquisitions respectively. Experimental results of these two types of experiment will be shown in this work.

The signal equation of a continuous object $\rho(\mathbf{r})$ for centric scan SPRITE is described as:

$$S(\mathbf{k}) = \int \rho(\mathbf{r}) e^{-\frac{t_p}{T_2^*(\mathbf{r})}} e^{-i2\pi\mathbf{k}\cdot\mathbf{r}} dr \qquad (10)$$
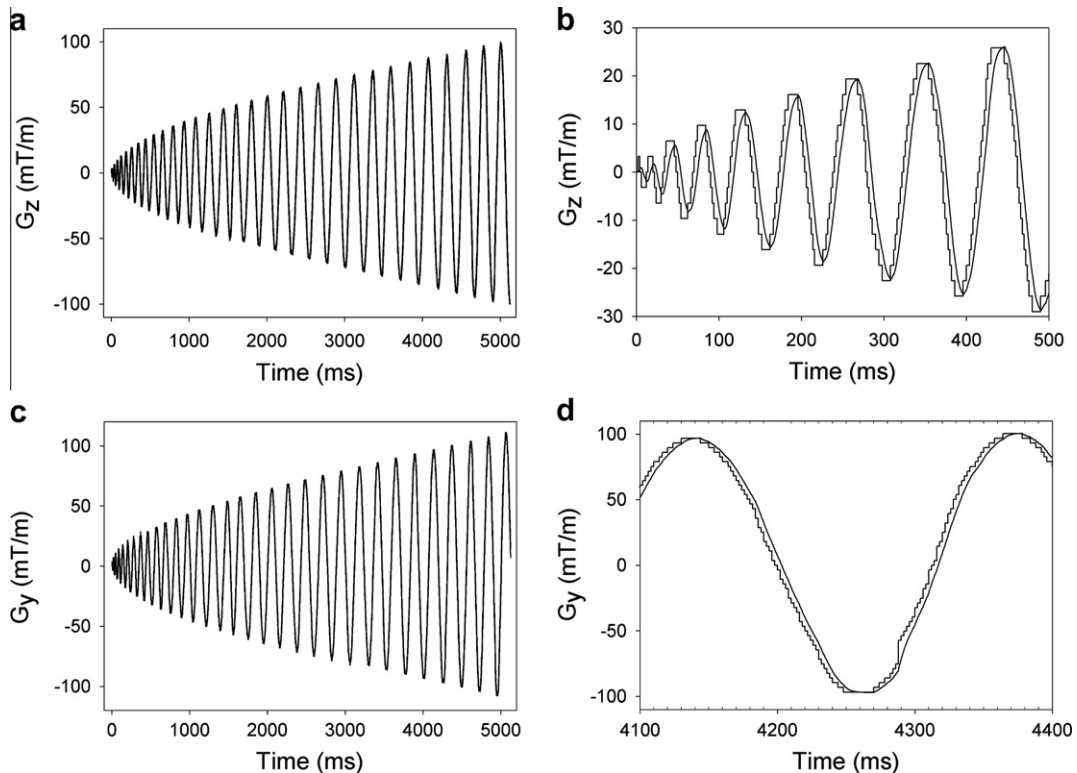

Fig. 3. MFGM monitored gradient waveforms for a single-shot Spiral SPRITE experiment compared with ideal waveforms. (a) Measured and ideal $G_z(t)$. (b) An expanded portion of (a). (c) Measured and ideal $G_y(t)$. (d) The expansion of (c) at a chosen time interval during the Spiral waveform. The ideal Spiral waveforms were discrete steps. The measurements show that the real waveforms were smoothed due to metal eddy current effects. High mutual inductance in the presence of the metal cell behaved as a low pass filter in the frequency domain.

where $T_2^*(r)$ is the apparent spin–spin relaxation time, and t_p the phase encoding time for spatially encoding spin magnetization following each broadband RF excitation. Variables **k** and **r** are the k-space and spatial vectors respectively.

In the presence of severe eddy currents or other magnetic field imperfections (e.g., the gradient delay, coupling between various gradient coils), image reconstruction can be performed based on the MFGM measured $\Delta B_0(t)$ field evolution and the gradient waveforms through conjugate phase reconstruction [27]:

$$\rho(\mathbf{r}) = \int S(\mathbf{k})w(\mathbf{k})e^{i2\pi\mathbf{k}\cdot\mathbf{r}}e^{i\gamma\Delta B_0(t)t_p}dk \qquad (11)$$

with $w(\mathbf{k})$ the k-space density compensation function and $\Delta B_0(t)$ the spatially-constant dynamic field. $w(\mathbf{k})$ is required to compensate for nonequidistant k-space samples. The density compensation is usually estimated from differences between adjacent k-space sample locations [25]. In 2D imaging Eq. (11) is extended as:

$$\rho(x,y) = \int\int S(k_x,k_y)w(k_x,k_y)e^{i\gamma t_p(G_x(t)\cdot x + G_y(t)\cdot y)}e^{i\gamma\Delta B_0(t)t_p}dxdy \qquad (12)$$

$B_0(t)$ eddy currents cause phase modulation of k-space data, which can be compensated by the phase demodulation of each k-space data point, as described by Eq. (12). In order to correct k-space misregistration, convolution gridding image reconstruction can be applied [28,29]. Alternatively, straightforward interpolation is possible [30,31]. In this work, interpolation followed by FFT was found to give high quality image reconstruction.

3. Results and discussion

3.1. Eddy currents in the metallic cell

Fig. 1 shows an aluminum vessel with a length of 15.2 cm, outer diameter of 7.6 cm, and a wall thickness of 1.3 cm. It fits smoothly into a standard micro imaging gradient bore (I.D $\approx$ 7.6 cm) and was centered along the B_0/G_z axis (error $\pm$ 1 mm) in a 2.4 T superconducting magnet.

The waveform measurement, Fig. 2, shows severe eddy current effects. A rectangular shape gradient pulse, with a duration of 50 ms and a nominal strength of 100 mT/m, was employed as a test waveform. The MFGM probehead was positioned at $z \approx \pm 1.5$ cm inside the sample space, to discriminate the linear eddy current effects from B_0 eddy current effects. The gradient rise time from 10% to 90% was as long as 10 ms due to the high electrical conductivity, and thickness, of the aluminum vessel walls. The natural rise time of the z gradient is less than 100 μs.

The measured B_0 eddy currents (<20 μT) were very small compared with linear eddy currents. They were less than 2% at a distance of 1 cm from the gradient isocenter. This results from the fact that the cell was symmetric and centered with respect to the gradient isocenter.

3.2. Spiral SPRITE imaging within metallic cells

3.2.1. Spiral SPRITE waveform monitoring using MFGM

Fig. 3 shows the gradient waveforms $G_z(t)$, $G_y(t)$ for a single-shot (one interleave) Spiral SPRITE acquisition. As illustrated, a commonly used single-shot 64×64 Spiral SPRITE acquisition acquires 2564 k-space data points in one interleaf. These points are sampled with a gradient step duration, TR, of 2 ms. The total duration of the gradient waveforms are thus as long as 5 s. Conventional methods [12–15] were unable to measure such long duration gradient waveforms due to sample T_2^* decay.

Unlike conventional methods [12–15], the MFGM method phase encodes the gradient amplitude by applying a train of closely spaced broadband RF excitations, in a way similar to the SPRITE

acquisition. As a consequence the FID single-point signal MFGM acquires is neither dephased by extended gradient waveforms, nor by high gradient strengths [16]. Based on Eqs. (7)–(9), MFGM was employed to monitor Spiral SPRITE gradient waveforms and the associated $B_0(t)$ field evolution in a sample space within the aluminum cell.

In this study the inside diameter of the aluminum cell is only 5.1 cm. The MFGM probehead was translated inside the aluminum cell and positioned at three locations with approximate (x, y, z) coordinates of (−0.8 cm, −1.0 cm, 1.6 cm), (1.0 cm, 1.0 cm, −1.5 cm), and (−0.8 cm, 1.2 cm, 1.6 cm), respectively. The small size of the MFGM RF probe monitor (<1 cm with RF shield) is advantageous in cases where the sample space of an MRI RF coil is restricted.

Since x, y gradient coils and the metal cell are both axially symmetric, the eddy current circulation patterns induced by $G_x(t)$ and $G_y(t)$ should be identical but different from that induced by $G_z(t)$. In order to study two different eddy current patterns, Spiral waveforms G_z, G_y were interrogated. Fig. 3 compares the differences between the monitored waveforms $G_z(t)$, $G_y(t)$ and the input waveforms. The metal induced eddy currents yield well-smoothed Spiral waveforms compared to the desired stepwise waveform.

3.2.2. Non-Cartesian sampled Spiral SPRITE imaging

As shown in Fig. 4, the monitored k-space trajectories for Spiral SPRITE were readily calculated from
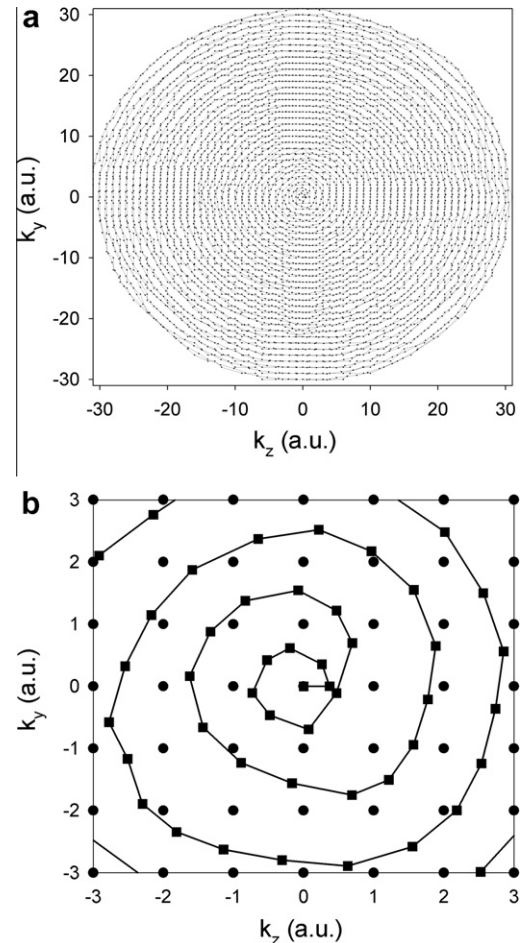

Fig. 4. The real k-space trajectory calculated based on Fig. 3 compared with the ideal trajectory. (a) Measured and desired k-space trajectories and associated k-space samples. The desired k-space samples (●) were restricted to Cartesian grids. Systematic differences between the two trajectories are apparent. (b) An expanded portion of (a) around the k-space center (ideal trajectory not shown). The measured k-space samples (■) deviate from Cartesian grid.

$$k(t) = \frac{\gamma}{2\pi} \int_0^{t_p} \mathbf{G}(\tau)d\tau = \frac{\gamma}{2\pi} \mathbf{G}(t)t_p \qquad (13)$$

where $\mathbf{G}(t) = [G_y(t), G_z(t)]$ is the average gradient amplitudes during the short phase encoding time t_p. It is clearly observed from the magnified Fig. 4b that in the presence of severe eddy currents, Spiral SPRITE k-space sampling is no longer Cartesian. Note the major errors in the data near the k-space origin. The discrepancies between desired and real k-space coordinates result in severe geometric distortion of the image without appropriate correction.

A cross-linked cis-polybutadiene resolution phantom Fig. 5a was employed to verify the possibility of correcting the major gradient waveform errors observed. The MR lifetimes of the material are $T_1 = 180$ ms, $T_2 = 640$ μs, and $T_2^* = 290$ μs.

The 2D Spiral SPRITE image in the presence of the metal cell is shown in Fig. 5b. As expected, the k-space misregistration caused by eddy currents led to severe image geometric distortion, image blurring, and errors in the quantification of the material. Note that the further from the center of the FOV, the greater the image distortion since eddy current effects increase with distance from the gradient origin. The k-space misregistration can be corrected by gridding the data points prior to image reconstruction according to Eq. (12). A cubic polynomial interpolation algorithm was applied to estimate the data on Cartesian grids based on the acquired data and the measured k-space locations.

The image after proper k-space registration is shown in Fig. 5c. The corrupted image due to linear eddy currents was successfully recovered. The quality of geometric features and quantification intensities after image correction are good. Residual image blurring

(e.g. the 1 mm holes) was typical for Spiral SPRITE experiments, and is primarily the result of discrete sampling (64×64) effects.

3.2.3. B_0 eddy current correction

The B_0 eddy currents, i.e., $B_0(t)$ field evolution, during Spiral scanning were also measured according to Eq. (7), as shown in Fig. 6. The oscillatory pattern of the monitored $B_0(t)$ field has the same periodicity as the Spiral gradient waveforms.

The induced B_0 eddy currents were found to be very small compared to linear eddy currents in the sample space. At the beginning of the Spiral scan (corresponding to the k-space center), B_0 eddy currents were found to be less than 5 μT, Fig. 6b. The $B_0(t)$ eddy currents cause static field B_0 temporal variation during SPRITE scanning, which modulates the SPRITE single-point signal with an additional phase during the phase encoding time t_p. The B_0 phase shifts for Spiral SPRITE k-space data were calculated through Eq. (14), and are shown in Fig. 6c.

$$\theta(k_n) = \int_0^{t_p} \gamma \Delta B_0(t')dt' = \gamma \Delta B_0(t'_n)t_p \qquad (14)$$

where $\Delta B_0(t'_n)$ denotes the average B_0 field offset during the short encoding time t_p at the nth k-space sampling.

Demodulation of erroneous phases can thus be readily implemented on a point-by-point basis in k-space, as described by Eq. (12). The final reconstructed phantom image using both monitored gradient waveforms and $B_0(t)$ field shifts is shown in Fig. 5d. After $B_0(t)$ phase correction, only slight improvements in the image, e.g.,
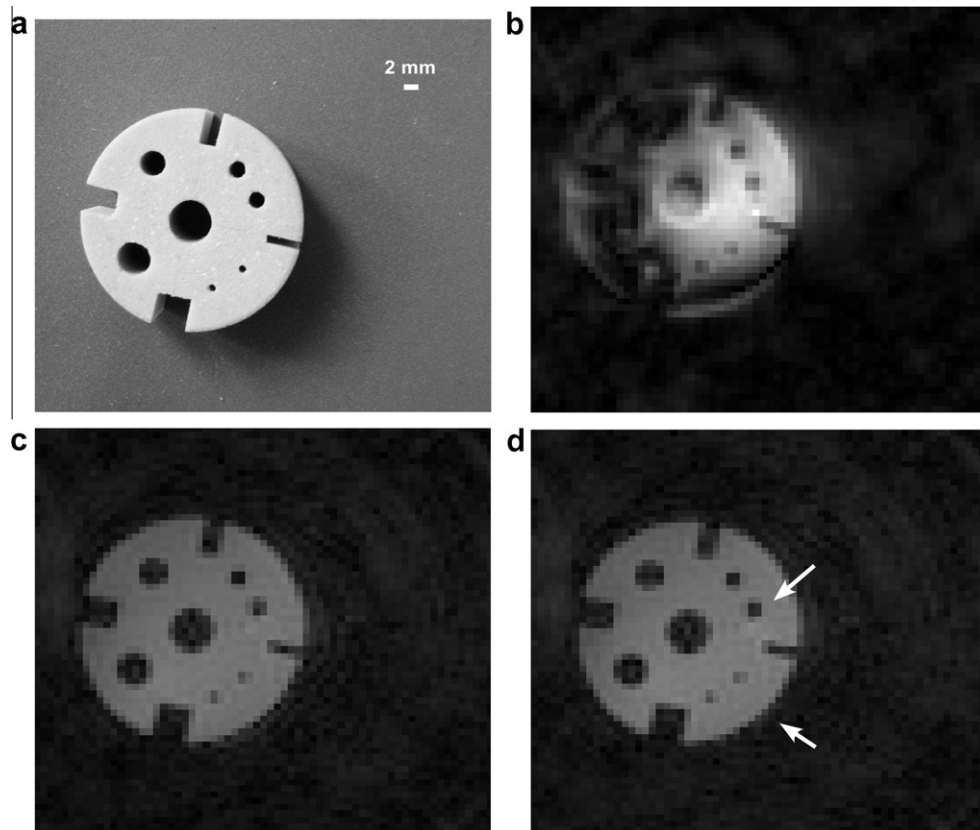

Fig. 5. Spiral SPRITE imaging of a resolution phantom inside an aluminum vessel. (a) Photo of the cross-linked cis-polybutadiene resolution phantom. The outer diameter is 25 mm and the thickness is 9 mm. The holes from large to small are 5 mm (center), 4 mm, 3 mm, and 1 mm in diameter, respectively. The widths of the four slots are 4 mm, 3 mm, 2 mm, and 1 mm, respectively. (b) 2D Spiral SPRITE image with the metal cell present, without any correction. Severe image geometric distortion, image blurring, and the errors in the quantification of the material were observed. (c) The image reconstructed using monitored gradient waveforms. A high quality image was successfully recovered. (d) The final reconstructed image using both monitored gradient waveforms and $B_0(t)$ field. Very slight improvements in the image quality, e.g., the deblurring at the places marked by arrows, were observed.
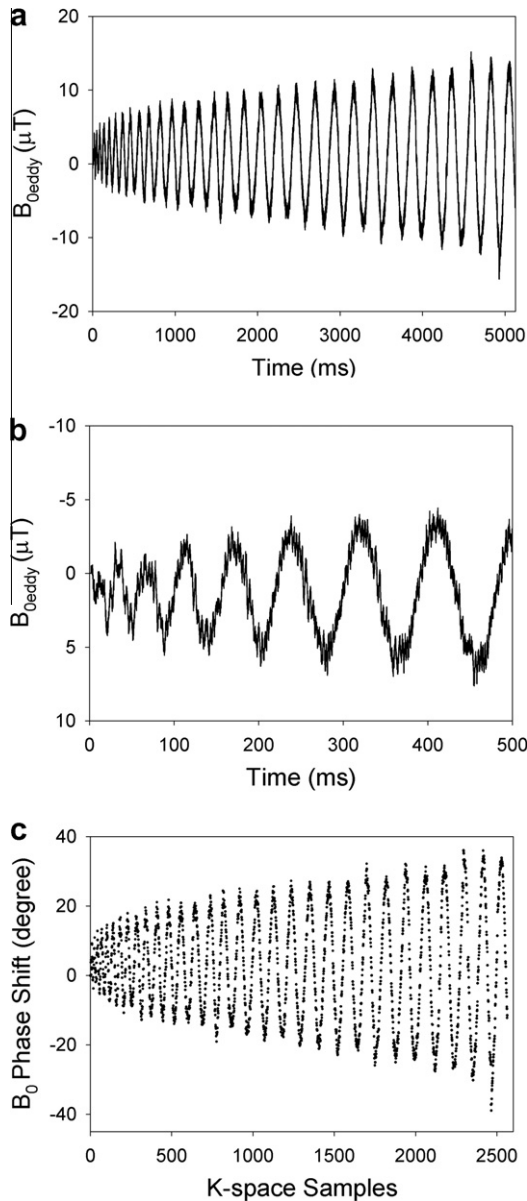
Fig. 6. Monitored $B_0(t)$ field evolution during Spiral SPRITE scanning. (a) The entire $B_0(t)$ field evolution. (b) An expansion of (a) at the beginning of the Spiral scan. (c) Calculated B_0 phase shifts for each Spiral k-space sample.

the deblurring at the places marked by arrows, were observed since the $B_0(t)$ eddy currents were not significant in this case.

3.3. 1D DHK SPRITE imaging with metallic cells

According to Eq. (1), in order to monitor 1D DHK SPRITE gradient waveform G_z the MFGM monitor was translated inside the aluminum cell and positioned at approximate z offsets of ±1.5 cm from the gradient isocenter, respectively. The measured waveform $G_z(t)$ was used to calculate the true k-space coordinates according to Eq. (13). The B_0 phase shifts for each k-space sample due to B_0 eddy currents were calculated from the monitored $B_0(t)$ field, as described by Eq. (14). DHK SPRITE imaging of a uniform gel phantom was undertaken with and without the metal cell.

In the absence of the metal cell, a homemade one-turn RF saddle coil was centered and supported by a plastic tube inside the gradient bore. The profile image of a gel phantom is reproduced

in Fig. 7a. The curved profile is a reflection of the B_1 inhomogeneity of the saddle RF probe. In the presence of the metal cell, the plastic tube was not employed and the DHK image is shown in Fig. 7b. The image is severely distorted due to eddy current effects. Similar to the image reconstruction for Spiral SPRITE, straightforward interpolation was applied to grid the k-space data. The $B_0(t)$ phase shifts were corrected on a point-by-point basis in k-space. The eddy current compensated images are shown in Fig. 7c and d. Note the slight differences appearing at the right and left extremes due to small B_0 effects. 1D DHK SPRITE image correction yields high quality images, as was the case with 2D Spiral SPRITE image correction. Linear eddy current and the B_0 eddy current effects are eliminated.

3.4. Nature of the metal

It should be noted that the imaging experiments were implemented with an end plate electrically connected to the cell (the far end of Fig. 1, thickness 1.27 cm). The end plate did not alter the large scale eddy current behavior in the sample space. This eddy current behavior is current circulating on the metal cylinder. It was concluded that the end plate effects are not a problem for MRI in the presence of metal vessels. For a vessel with a length of 15.2 cm and the geometry of Fig. 1, the spatial extent of linear gradient fields was more than 5 cm, which is longer than the homogeneous B_1 range (5 cm) of the RF coil.

The metal cylinder was positioned symmetrically with respect to all three physical gradient axes therefore the eddy current components induced by all three orthogonal gradients are mainly linear eddy currents. The accuracy in centering the vessel along B_0/G_z is not a strict requirement (∼1 mm). Higher-order non-linear eddy currents as described in Eq. (1) were negligible as manifest in pure phase encode SPRITE imaging. Although in principle the measurements and correction of high-order eddy currents are possible with MFGM, the added complexity arising from characterizing and compensating non-linear gradient fields would hinder what is otherwise a simple and straightforward procedure.

The material of the cell in this work was chosen to be aluminum due to its easy machining. Aluminum has a high electrical conductivity of 37.8×10^6 S m^{-1} [32]. Other applicable metal alloys include non-magnetic stainless steel and titanium. Both titanium and steel have electrical conductivities an order of magnitude less than aluminum. The metal induced eddy currents are proportional to the electrical conductivity of the metal as described by Eq. (15) [33].

$$\tau = K\sigma\mu\Gamma \tag{15}$$

where τ is the eddy current time constant, σ and μ are the conductivity and permeability of the conductor respectively, Γ represents a specific geometry, and K is a constant value. The metals of interest have similar permeability. Therefore the eddy currents induced by steel and titanium will be less than for aluminum and should be readily corrected with the proposed strategy.

As suggested by an anonymous reviewer it would be possible to employ a long repetition time SPI experiment to image samples in vessels such as those described in this paper. In such an experiment it would not be necessary to wait for gradients to fully stabilize [39], but the acquisition time would be lengthy and the gradient duty cycle problematic.

4. Conclusion

Magnetic field gradient waveform monitoring (MFGM) with $B_0(t)$ field measurement has been proposed for MRI inside metallic vessels. The essential problem, eddy currents circulating in the metal, was overcome in this work which employed a simple alumi-
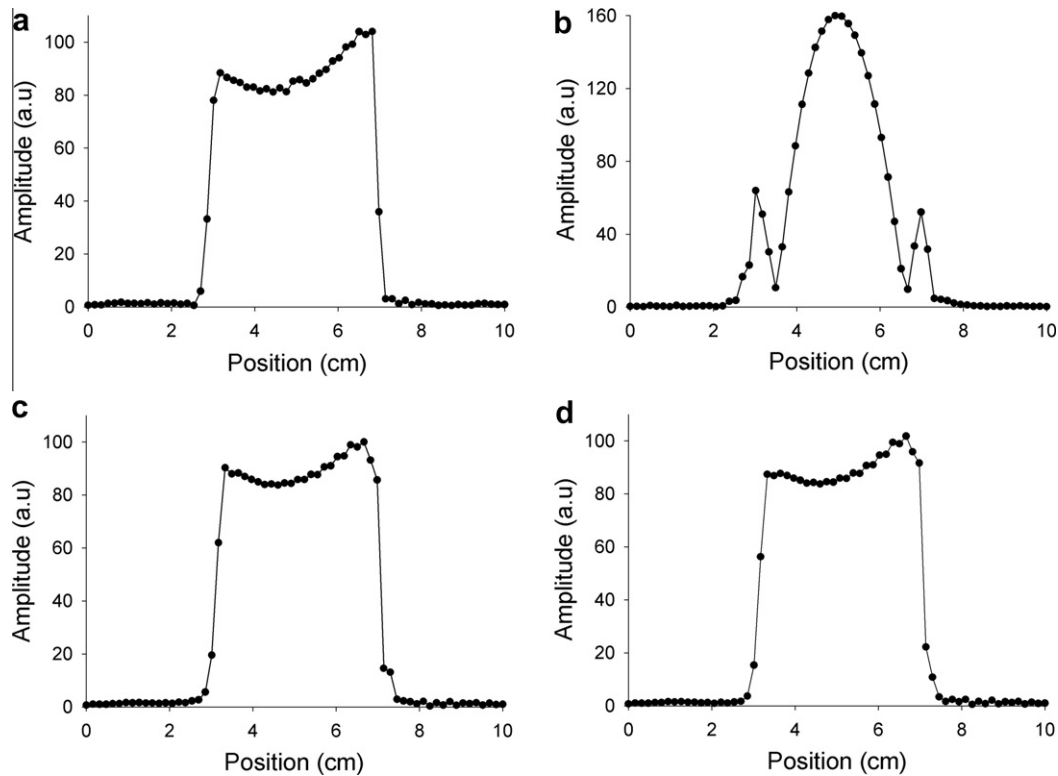
Fig. 7. 1D DHK SPRITE imaging (z direction) of a uniform gel phantom within the aluminum cell. (a) Template image acquired without the metal cell. The curved profile is a reflection of the B_1 inhomogeneity of our homebuilt saddle RF coil. (b) Corrupted image acquired with the metal cell present. (c) The reconstructed DHK SPRITE image with correction of linear eddy current effects. (d) The reconstructed DHK SPRITE image with correction of linear eddy current and B_0 eddy current effects. Note the slight differences at the right and left extremes in (c) and (d) due to $B_0(t)$ effects.

num cell. Quantitative centric scan SPRITE imaging including 1D DHK and 2D Spiral acquisitions were undertaken in the presence of the aluminum cell.

Gradient switching induced eddy currents in the aluminum vessel were measured and analyzed with the improved MFGM method. The Spiral SPRITE gradient waveforms were temporally mapped inside the metal cell using a small MFGM probe monitor. Simultaneous $B_0(t)$ field evolution during Spiral SPRITE scanning was also measured and $B_0(t)$ eddy currents were found to be very small with the cell centered inside the gradient coil.

An interpolation gridding image reconstruction was used to correct the misregistered k-space data caused by linear eddy currents. $B_0(t)$ phase shifts resulting from B_0 eddy currents were corrected on a point-by-point basis in k-space. Gridding image reconstruction using monitored gradient waveforms provides images of high quality. The image was slightly improved with B_0 eddy current correction using the monitored $B_0(t)$ field. Higher-order eddy currents were negligible as manifest in pure phase encode SPRITE imaging. We believe this work will lead to MRI compatible metallic pressure vessels in the near future. This ability will open entirely new vistas of study for material science MR and MRI.

It should be pointed out that the features of MFGM, e.g., the small size of the monitor probe, are desirable for pre-clinical small animal imaging and magnetic resonance spectroscopy (MRS) [34,35]. This study is also beneficial to evaluation and reduction of RF probe related eddy currents [36]. The MFGM method may also be used to study gradient induced eddy current effects for near implant imaging [37,38].

5. Experimental

All gradient waveform mapping and imaging experiments were implemented on a Nalorac (Martinez, CA) 2.4 T, 32 cm i.d horizon-

tal bore superconducting magnet. The cylindrical aluminum cell (Fig. 1) was tightly fit in a commercial water-cooled 7.6 cm i.d. gradient set, driven by a Techron (Elkhart, IN) 8710 amplifier, providing a maximum gradient strength of 250 mT/m. The imaging RF coil inside the cell was a homebuilt eight-rung single mode birdcage, which had an inside diameter of 3 cm and a homogeneous B_1 field range of 5 cm. The imaging RF probe is located inside the metal vessel and is therefore altered in tuning by the presence of the vessel, but otherwise functions as an ordinary RF probe. This is readily understood if one considers the metal vessel to be an RF shield for the probe. It is a more substantial shield than normal, but still an RF shield. The probe was driven by a 2 kW AMT (Brea, CA) 3445 RF amplifier. The MRI hardware system was controlled by a Tecmag (Houston, TX) Apollo console.

The magnetic field gradient waveform monitor probe was described in [16]. The single turn solenoid had a 90° pulse length of 5 μs and a deadtime of 10 μs. The MFGM probehead was connected to a rigid coaxial cable as a support. The water drop test sample within the MFGM probe had relaxation times T_2^*, T_2, and T_1 of less than 100 μs due to doping with a high concentration of GdCl$_3$.

For the Spiral SPRITE waveform measurements, the MFGM probehead was positioned at three different locations within the cell. In the waveform mapping sequence [16], the chosen time interval between consecutive RF pulses was 320 μs. The RF pulse duration was 2 μs for a flip angle of 36°. The experimental waveform temporal resolution was 64 μs/point. The phase encoding time was 40 μs with 64 averages collected for a scan time of 27 min at each MFGM probe location. Two separate calibration measurements (for y_i/y_j and z_i/z_j) were executed at each probe location, with each lasting 30 s. Since T_1 of the test sample is on the order of 100 μs, the calibration scan was very rapid. The total calibration time for all three MFGM locations was 3 min. The complete waveform measurement time was almost 90 min since the Spiral SPRITE waveform duration is 5 s.

All Spiral SPRITE images acquired were 64×64 with a field of view (FOV) of 5 cm $\times$ 4.5 cm in the G_z and G_y directions, respectively. The encoding time and the flip angle were 150 μs and 3°, respectively. The experiment time for 2D Spiral SPRITE was approximately 2 min. A 2D cubic polynomial interpolation algorithm was written in MATLAB 7.0 (the MathWorks, Natick, Massachusetts, USA) for gridding k-space data. MATLAB 7.0 was also used in reconstructing Spiral SPRITE images and related data processing.

The 1D DHK SPRITE images had a FOV of 10 cm in the G_z direction. The encoding time and the flip angle were 90 μs and 18°, respectively. The experiment time for DHK SPRITE was approximately 25 s for 64 averages. The uniform gel phantom, doped with $GdCl_3$, had T_2^*, T_2, and T_1 s of approximately 300 μs. A 1D quadratic polynomial interpolation gridding algorithm was written in IDL (Research Systems, Boulder, CO). IDL was also used for data processing related to gradient waveform mapping.

References

[1] B. Benedek, M.J. Purcell, Nuclear magnetic resonance in liquids under high pressure, Chem. Phys. 22 (1954) 2003–2012.
[2] J.D. Grunwaldt, R. Wandeler, A. Baiker, Supercritical fluids in catalysis: opportunities of in situ spectroscopic studies and monitoring phase behavior, Catal. Rev. 45 (2003) 1–96.
[3] W.J. Sprengers, A.M. Kluwer, S. Gaemers, C.J. Elsevier, High-pressure NMR spectroscopy: some general aspects and applications, Defect Diffus. Forum 208–209 (2002) 283–294.
[4] W. Kremer, M.R. Arnold, N. Kachel, H.R. Kalbitzer, The use of high-sensitivity sapphire cells in high pressure NMR spectroscopy and its application to proteins, Spectrosc. Int. J. 18 (2004) 271–278.
[5] K.J. Thurecht, D.J.T. Hill, A.K. Whittaker, Equilibrium swelling measurements of network and semicrystalline polymers in supercritical carbon dioxide using high-pressure NMR, Macromolecules 38 (2005) 3731–3737.
[6] B.A. Baldwin, J. Stevens, J.J. Howard, A. Graue, B. Kvamme, E. Aspenes, G. Ersland, J. Huseb, D.R. Zornes, Using magnetic resonance imaging to monitor CH_4 hydrate formation and spontaneous conversion of CH_4 hydrate to CO_2 hydrate in porous media, Magn. Reson. Imaging. 27 (2009) 720–726.
[7] R.H. Morris, M. Bencsik, N. Nestle, P. Galvosas, D. Fairhurst, A. Vangala, Y. Perrie, G. McHale, Robust spatially resolved pressure measurements using MRI with novel buoyant advection-free preparations of stable microbubbles in polysaccharide gels, J. Magn. Reson. 193 (2008) 159–167.
[8] L. Li, Q. Chen, A.E. Marble, L. Romero-Zerón, B. Newling, B.J. Balcom, Flow imaging of fluids in porous media by magnetization prepared centric-scan SPRITE, J. Magn. Reson. 197 (2009) 1–8.
[9] S. Gaemers, C.J. Elsevier, Reducing the NMR line widths of quadrupole nuclei by employing supercritical solvents, Chem. Soc. Rev. 28 (1999) 135–141.
[10] P. Blumler, B. Blumich, R. Botto, E. Fukushima, Spatially Resolved Magnetic Resonance: Methods, Materials, Medicine, Biology, Rheology, Geology, Ecology, Hardware, Wiley-VCH, Weinheim, 1998.

[11] B. Blumich, NMR Imaging of Materials, Oxford University Press, Oxford, 2000.
[12] A. Takahashi, T. Peters, Compensation of multi-dimensional selective excitation pulses using measured k-space trajectories, Magn. Reson. Med. 34 (1995) 446–456.
[13] G. Mason, T. Harshbarger, H. Hetherington, A method to measure arbitrary k-space trajectories for rapid MR imaging, Magn. Reson. Med. 38 (1997) 492–496.
[14] J.H. Duyn, Y.H. Yang, J.A. Frank, Simple correction method of k-space trajectory deviations in MRI, J. Magn. Reson. 132 (1998) 150–153.
[15] N. De Zanche, C. Barmet, J.A. Nordmeyer-Massner, K.P. Pruessmann, NMR probes for measuring magnetic fields and field dynamics in MR systems, Magn. Reson. Med. 60 (2008) 176–186.
[16] H. Han, R. MacGregor, B.J. Balcom, Pure phase encode magnetic field gradient monitor, J. Magn. Reson. 201 (2009) 212–217.
[17] I.V. Mastikhin, B.J. Balcom, P.J. Prado, C.B. Kennedy, SPRITE MRI with prepared magnetization and centric k space sampling, J. Magn. Reson. 136 (1999) 159–168.
[18] M. Halse, D.J. Goodyear, M.B. MacMillan, P. Szomolanyi, D. Matheson, B.J. Balcom, Centric scan SPRITE magnetic resonance imaging, J. Magn. Reson. 165 (2003) 219–229.
[19] M. Halse, J. Rioux, S. Romanzetti, J. Kaffanke, B. MacMillan, I. Mastikhin, N.J. Shah, E. Aubanel, B.J. Balcom, Centric scan SPRITE magnetic resonance imaging: optimization of SNR, resolution and relaxation time mapping, J. Magn. Reson. 169 (2004) 102–117.
[20] L. Li, H. Han, B.J. Balcom, Spin echo SPI methods for quantitative analysis of fluids in porous media, J. Magn. Reson. 198 (2009) 252–260.
[21] K. Deka, B. MacMillan, G.R. Ziegler, A.G. Marangoni, B. Newling, B.J. Balcom, Spatial mapping of solid and liquid lipid in confectionery products using a 1D centric SPRITE MRI technique, Food Res. Int. 39 (2006) 365–371.
[22] U. Setthanan, B. MacMillan, S. McGrady, Spatially resolved hydrogen desorption from aluminum hydride observed by magnetic resonance imaging, Int. J. Hydrogen Energy 34 (2009) 8067–8072.
[23] Z.H. Zhang, A.V. Ouriadov, C. Willson, B.J. Balcom, Membrane gas diffusion measurements with MRI, J. Magn. Reson. 176 (2005) 215–222.
[24] S. Gravina, D.G. Cory, Sensitivity and resolution of constant-time imaging, J. Magn. Reson. B 104 (1994) 53–61.
[25] M.A. Bernstein, K.F. King, X.J. Zhou, Handbook of MRI Pulse Sequences, Elsevier Academic Press, Burlington, 2004.
[26] D.B. Twieg, The k-trajectory formulation of the NMR imaging process with applications in analysis and synthesis of imaging methods, Med. Phys. 10 (1983) 610–621.
[27] A. Macovski, Volumetric NMR imaging with time-varying gradients, Magn. Reson. Med. 2 (1985) 29–40.
[28] J. O(Sulllivan, A fast sinc function gridding algorithm for Fourier inversion in compute tomography, IEEE Trans. Med. Imaging 4 (4) (1985) 200–207.
[29] P.J. Beatty, D.G. Nishimura, J.M. Pauly, Rapid gridding reconstruction with a minimal oversampling ratio, IEEE Trans. Med. Imaging 24 (6) (2005) 799–808.
[30] H. Stark, J.W. Woods, I. Paul, R. Hingorani, An investigation of computerized tomography by direct Fourier inversion and optimum interpolation, IEEE Trans. Biomed. Eng. 28 (7) (1981) 496–505.
[31] S.X. Pan, A.C. Kak, A computational study of reconstruction algorithms for diffraction tomography – interpolation versus filtered backpropagation, IEEE Trans. Acoust. Speech Sig. Proc. 31 (1983) 1262–1275.
[32] R.C. Weast, Handbook of Chemistry and Physics, CRC Press, Cleveland, 1976.
[33] R.L. Stoll, The Analysis of Eddy Currents, Clarendon Press, Oxford, 1974.
[34] I. Tkac, Z. Starcuk, I.Y. Choi, R. Gruetter, In vivo ^1H NMR spectroscopy of rat brain at 1 ms echo time, Magn. Reson. Med. 41 (1999) 649–656.
[35] N. Braakman, T. Oerther, H.J.M. de Groot, A. Alia, High resolution localized two-dimensional MR spectroscopy in mouse brain in vivo 60 (2008) 449–456.
[36] M. Alecci, P. Jezzard, Characterization and reduction of gradient-induced eddy currents in the RF shield of a TEM resonator, Magn. Reson. Med. 48 (2002) 404–407.
[37] A. Shenhav, H. Azhari, Gradient field switching as a source for artifacts in MR imaging of metallic stents, Magn. Reson. Med. 52 (2004) 1465–1468.
[38] S.H. Kolind, A.L. MacKay, P.L. Munk, Q.S. Xiang, Quantitative evaluation of metal artifact reduction techniques, J. Magn. Reson. Imaging 20 (2004) 487–495.
[39] B.J. Balcom, M. Bogdan, R.L. Armstrong, Single point imaging of gradient rise, stabilization and decay, J. Magn. Reson. A 118 (1996) 122–125.